GeoHazards

MDPI

Article

Cross-Validated Geophysical Profiling of the Novi Han Fault: Insights into Segmented and Characteristic Rupture Behavior in the Sofia Basin

Alexander Radulov [1,*], Emil Oynakov [2], Yordanka Donkova [1], Lyubka Pashova [2], Petar Kirilov [2] and Radan Ivanov [2]

[1] Geological Institute, Bulgarian Academy of Sciences, Acad. G. Bonchev St., bl. 24, 1113 Sofia, Bulgaria; dani@geology.bas.bg
[2] National Institute of Geophysics, Geodesy and Geography, Bulgarian Academy of Sciences, Acad. G. Bonchev St., bl. 3, 1113 Sofia, Bulgaria; emil.oinakov@geophys.bas.bg (E.O.); lpashova@geophys.bas.bg (L.P.); petarhristovkirilov@geophys.bas.bg (P.K.); rivanov@geophys.bas.bg (R.I.)
* Correspondence: radulov@geology.bas.bg

Abstract

To refine active fault mapping in the Sofia Basin in Bulgaria, we investigate the near-surface geology of the Novi Han fault segment by integrating topographic profiling of the fault scarp, electrical resistivity tomography, and vertical-component microseismic standing-wave data. Topographic morphometry reveals a compound scarp with 7 m of vertical offset, where scarp crest retreat indicates long-term degradation following the last surface-rupturing earthquake. Co-located resistivity and standing-wave models independently image a north-dipping fault that separates Neogene sand strata in the footwall from fine-grained Quaternary deposits in the hanging wall. This model correspondence illustrates how standing-wave modeling can resolve spatial variations in fluid saturation and elastic impedance into a reliable pseudo-depth profile that aligns well with physical depth when constrained by a reliable Vp model. Microseismic intensity distributions reveal a sub-fault wavefield focusing effect that enhances fault-plane resolution at depths exceeding the penetration limits of resistivity imaging. When synthesized with earthquake records, our results indicate that the Novi Han fault segment likely did not rupture in the 1858 Mw6.2 earthquake. Seismic hazard models for the Sofia Basin should therefore incorporate partial-rupture scenarios alongside system-wide characteristic events to account for structural fault heterogeneity.

Keywords: active faulting; electrical resistivity tomography; ambient-noise standing waves; microseismic resonance; fault-zone imaging; passive seismic methods; Sofia Basin

Check for updates

Academic Editor: Yuchen Wang

Received: 23 September 2026
Revised: 11 November 2026
Accepted: 25 November 2026
Published: 28 November 2026

Copyright: © 2026 by the authors. Licensee MDPI, Basel, Switzerland. This article is an open access article distributed under the terms and conditions of the Creative Commons Attribution (CC BY) license.

1. Introduction

Kanev [1,2] mapped an ~15-km-long fault scarp in young unconsolidated sediments in the southeastern vicinity of Sofia, Bulgaria. This early discovery provides observational constraints for parameterizing fault sources in modern seismic hazard models. The fault segment accommodates strain within a broader extensional regime where large shallow earthquakes recur over long intervals. The Sofia basin is a locus of continental extension [3–7] within the northernmost Aegean domain (e.g., [8,9]) since the late Miocene [10,11] (Figure 1a). The Sofia faults, whose geometry and kinematics are influenced by inherited structural heterogeneity within the Balkanide orogen, accommodate

approximately N–S extension driven by far-field Hellenic slab roll-back and gravitational potential energy contrasts [12,13].

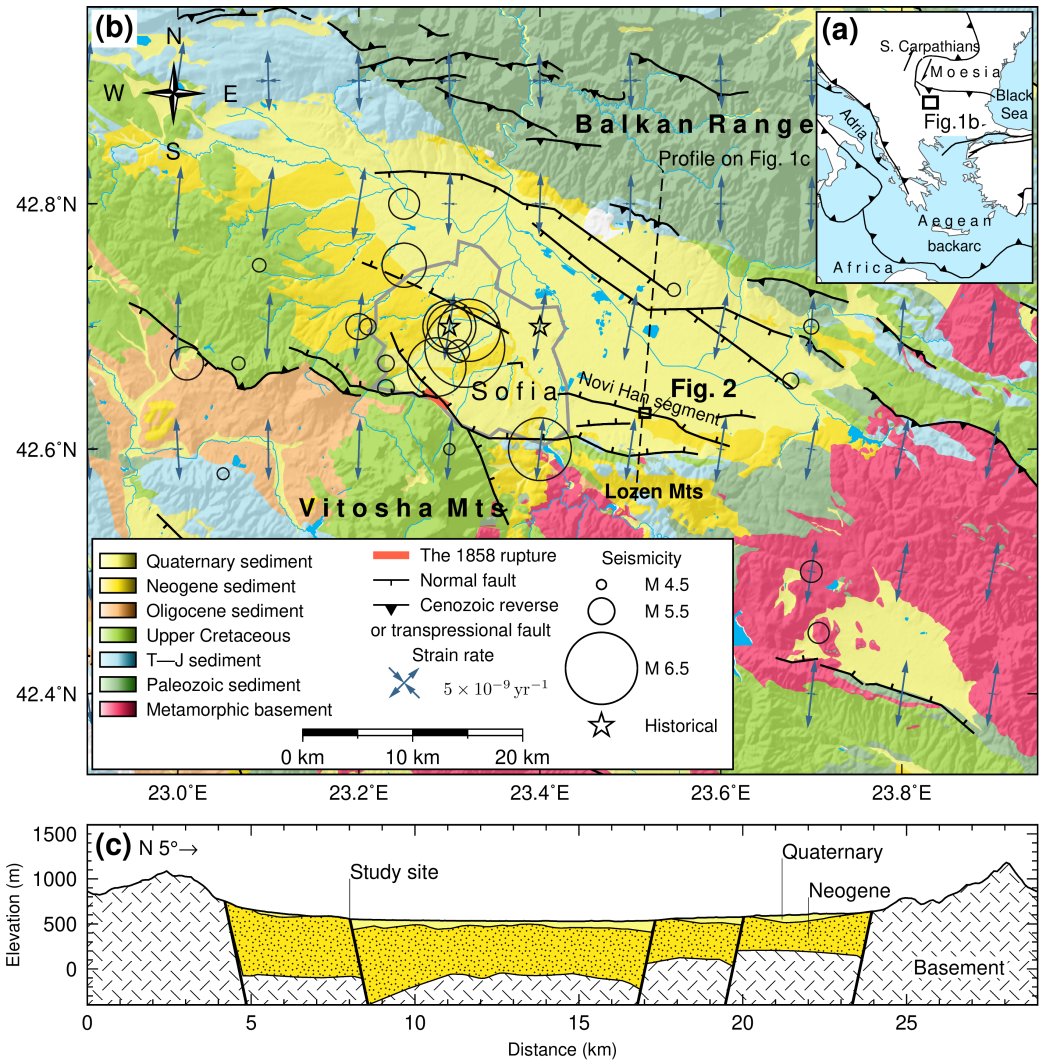

Figure 1. Regional tectonic setting for the Sofia area; adapted from Radulov et al. [7,14], Oynakov et al. [15]. (**a**) Location of the target area in the Eastern Mediterranean. (**b**) Main geological units of the Sofia region, combined with earthquake epicenters from 1450 to 2014 [16] and strain rate field derived from GNSS velocities [13]. The box on the Novi Han fault segment marks the coverage of Figure 2, and the dashed line indicates the profile trace shown on panel (**c**). (**c**) Geological cross-section profile illustrating the graben relationships between basement, Neogene, and Quaternary sedimentary units, with the study site indicated.

Minimal progress in fault mapping at the field scale in the Sofia basin [7,17] since the foundational work of Kanev [1,2] leaves seismogenic faults without precise spatial constraints. Rapid urbanization over recent decades obscures tectonic landforms and heightens the need for site-specific investigations on preserved fault scarps. To meet this need, our study examines the fault segment documented by Kanev–herein designated the Novi Han fault segment.

In a recent passive seismic investigation across the Novi Han fault segment using ambient-noise spectral profiling, Oynakov et al. [18] delineated the fault based on changes in spectral amplitude, directional wavefield behavior, and horizontal polarization oriented nearly perpendicular to the fault strike. Here, we expand their investigation incorporating topographic and electrical resistivity profiles. While topographic and resistivity profiling re-

liably resolve the morphological and geological traces of past surface-rupturing earthquakes (e.g., [7,19,20]), passive seismic methods remain experimental in reaching equivalent spatial resolution at the site scale (e.g., [21]).

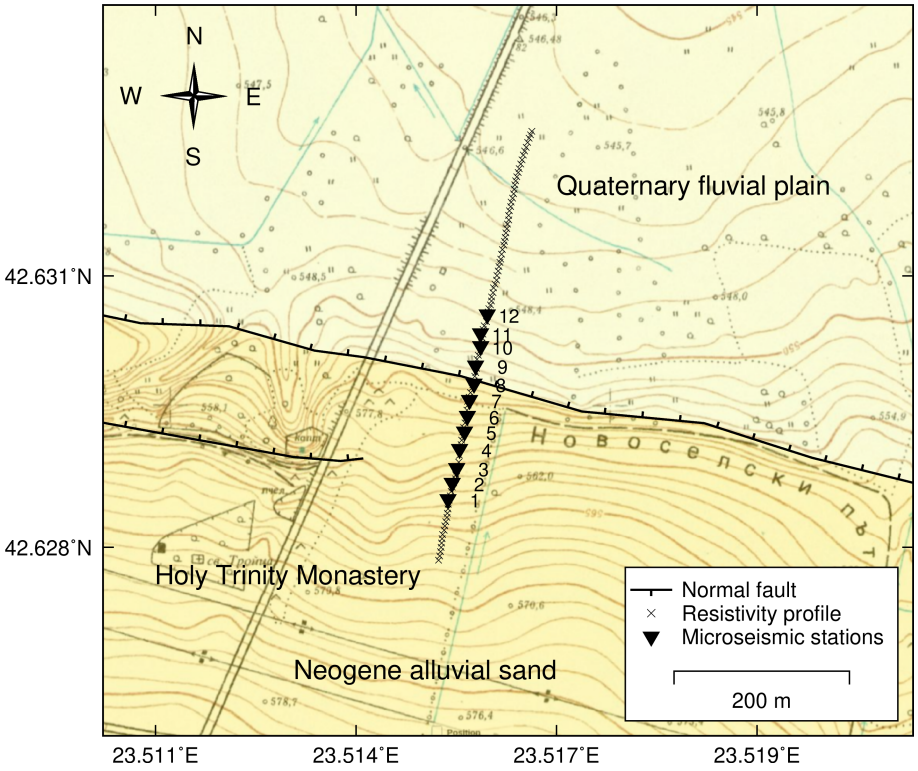

Figure 2. Location of microseismic sounding stations (1–12) and resistivity profile across the Novi Han fault segment over a 1:5000 topographic map with a 1 m contour interval.

Near-surface geophysical imaging, particularly electrical resistivity tomography and passive seismic profiling in unconsolidated sedimentary environments, suffers from inherent non-uniqueness, because inverse models yield multiple geological interpretations that satisfy the same observational data (e.g., [22,23]). In this study, we combine co-located resistivity profiling and passive microseismic resonance profiling to image fault zone at shallow depth. Resistivity and passive seismic measurements respond to different physical properties of the subsurface. Their comparison provides an independent geophysical constraint on the interpretation and reduces the ambiguity inherent in either dataset considered alone. Subsurface resistivity depends on lithology, fluid saturation and pore-fluid salinity. However, utilizing short electrode spacings for higher resolution limits the depth of investigation, typically restricted to the shallow tens of meters depending on array geometry. Passive microseismic profiling provides complementary information on the spatial variability of the ambient seismic wavefield and may extend the investigation beyond the depth of shallow resistivity imaging. The passive seismic standing-wave method is based on the extraction of persistent standing-wave components from ambient seismic noise by averaging or accumulating amplitude spectra of a large number of noise records [24–27]. Compressional standing waves can develop through interference between incident and reflected waves where sufficiently strong contrasts in acoustic impedance are present within the near-surface medium [24,27]. Here, we evaluate whether spatial variations in the vertical-component ambient-noise spectrum can delineate shallow subsurface geology across the fault zone. We focus on the frequency, relative amplitude, and lateral continuity of stable spectral peaks and bands rather than attempting to reconstruct complete standing-wave mode shapes. Integrated physical datasets reduce non-uniqueness. This joint approach

provides the necessary preliminary insight into the subsurface geology beyond the depth and resolution limits of individual methods.

Here, we combine high-precision field GNSS-RTK topographic profiling measured every 5 m with millimeter-scale accuracy, electrical resistivity profiling utilizing a minimum electrode spacing of 5 m, and reprocessed vertical-component ambient-noise recordings collected across the Novi Han fault segment by Oynakov et al. [18]. We first describe the fault scarp morphometry and present a shallow subsurface resistivity model along with its geological interpretation. We then analyze the stability, frequency, relative amplitude, and spatial distribution of persistent spectral features in the ambient-noise recordings. We compare the resistivity model and normalized spectral amplitude pseudo-section with the microseismic intensity model of Oynakov et al. [18] to determine which subsurface boundaries are supported by independent geophysical measurements and which may reflect wavefield-specific effects. Finally, we place our findings into the broader context of the Sofia Basin to discuss the plausibility of partial ruptures versus full-system ruptures in terms of fault behavior.

2. Geologic Setting

2.1. Pre-Neogene Basement

The Sofia sedimentary basin occupies an intramontane depression in the Balkanides orogen, bounded by diverse pre-Neogene lithological units [28,29]. Ordovician to Permian sedimentary sequences dominate the northern nappe units along the Balkan Range and eastern basin margins (Figure 1). Late Cretaceous volcanic-arc assemblages bound the southern margin and constitute the underlying bedrock of the basin. Surrounding uplifts additionally expose Triassic and Jurassic clastic and carbonate sequences, which extend beneath the northern part of the basin.

Regional compressional deformation culminated during the Eocene (48–37 Ma), when thrusting displaced nappes northward onto the Moesian Platform [30–34]. Strain partitioning among strike-slip and reverse faults during the Eocene oblique convergence [35] established structural precursors that governed subsequent fault reactivation in the Sofia region.

2.2. Neogene to Quaternary Basin Evolution and Stratigraphy

The tectonic shift toward extensional dominance during the middle–late Miocene (13.8–7.2 Ma) is recorded by drainage network rearrangement and the onset of Vitosha Mountains uplift [36]. Deposition in the basin initiated during the late Miocene (Meotian, 7.4–6.1 Ma) [10]. Tectonic subsidence accommodated a sedimentary sequence averaging 500–600 m in thickness, while concurrent uplift raised adjacent ranges over 1500 m above the basin floor (Figure 1c) [36]. Range-front retreat preceding Neogene deposition allowed the basin to expand partially onto fault footwalls [7,10]. Throughout graben development, the transverse Iskar River system drove basin depositional dynamics, supplying most of the sediment via a succession of superimposed fluvial fans and fan deltas [7,37].

Late Miocene to Pliocene stratigraphy is controlled by lateral transitions from the main Iskar fluvial fan to smaller alluvial fans fed by adjacent catchments [10,11]. Formal lithostratigraphic nomenclature defines the basal unit as the Variegated Terrigenous Formation (Figure 3) [10]. During the Pontian–Dacian times, lacustrine fan-delta deposits of the Novi Iskar Formation accumulated coevally with surrounding fluvial and alluvial fan sequences of the Gnilyane and Lozenets formations [10,38].

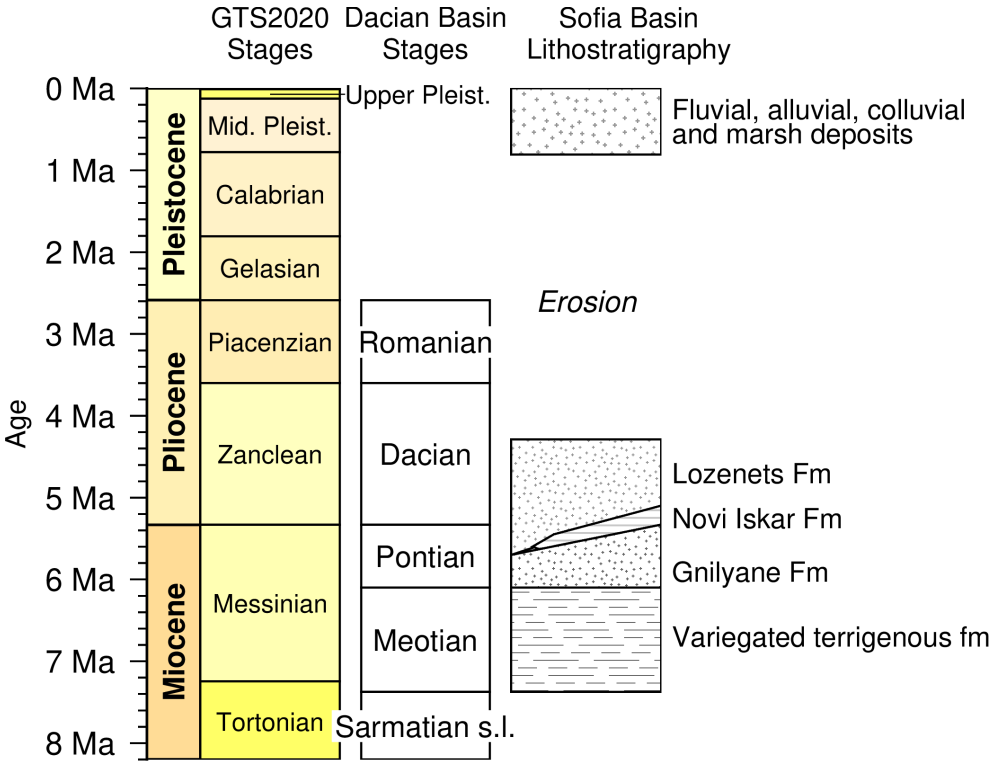

Figure 3. Lithostratigraphic chart for the Sofia Basin [10], aligned with the international Geological Time Scale (GTS2020) [39,40] and regional Dacian Basin stages (Paratethys) [41,42].

Following a period of erosion, fluvial and alluvial fan deposition recommenced during the Quaternary. Pediments and deeply incised mountain channels indicate that erosion continued to dominate Quaternary landscape evolution [7].

2.3. Fault Architecture and Contemporary Geodynamics

Various tectonic models have been proposed to explain the basin-and-range morphology of the Sofia region using field observations, borehole logs [10,28,43], and geophysical surveys [44]. Early interpretations categorized the basin as a half-graben [30,45], a simple graben bounded solely by continuous range-front faults [6,8,46], a complex graben containing interior faults [3,4,7,28,47], or a dense network of cross-cutting faults [5,48,49]. Integrated geophysical [7,15,44] and borehole data [10,28,43] best support a framework of two antithetic fault systems incorporating step-overs, overlaps, and variable-strike branches (Figure 1) [4,7,28,43,47].

Ongoing extension across the Sofia region maintains a uniform strain rate field, with the principal extensional eigenvalue averaging 7×10^{-9} yr^{-1} [13,50,51] (Figure 1b). Faults that strike oblique to the regional extension direction accommodate the ongoing strain (Figure 1b).

Since 1450, twelve large earthquakes have been documented in the Sofia Basin (Figure 1b). Data constraints preclude magnitude assignment for the 1450, 1749, and 1848 historical events. Five M_w 6.1–6.5 events occurred between 1557 and 1858, and four M_w 5.5–5.9 events followed between 1858 and 1895 [16]. Except for the 1858 event, which is historically associated with the southern fault system [52], specific fault source assignments for earlier historical earthquakes remain unknown. Elevated radon and hydrogen soil-gas emissions have been recorded near the reported 1858 surface fault rupture [53,54]. Since 1895, background seismicity ($M_w < 5.5$) clusters within the hanging wall of the fault that ruptured in 1858 and in the northeastern basin [55].

No paleoseismic constraints currently exist to quantify site-specific recurrence intervals between large earthquake. Paleoseismological studies on adjacent extensional faults indicate that recurrence intervals range from approximately 2000 to over 10,000 years [56–58].

3. Study Site and Methods

3.1. Study Site

The study site is situated in the central portion of the Novi Han fault segment. The Novi Han fault segment has a frontal position in two overlapping segments that form the southern fault system to the east (Figure 1b). Fault scarps and outcropping fault planes trace the rear fault segment near the Iskar inlet, whereas no corresponding evidence is preserved farther west along the Lozen Mts front. (Refs. [1,2] and own observations). The presence of a relay ramp stepping toward the frontal fault segment indicates a transfer zone adjacent to the study site (Figure 1b). Strain transfer is additionally evidenced by sedimentary distribution. The Lozenets Formation, exposed or capped by thin Quaternary colluvium within the relay ramp and the eastern Novi Han footwall, records long-term uplift. In response to subsidence, Quaternary sediments in the hanging wall of the fault accumulated to a thickness exceeding 250 m [43,49]. Quaternary deposition encompasses the east-prograding Iskar alluvial fan, an axial river to the north, alluvial fans along the Lozen Mountains front, and fault-scarp colluvium, all of which form a dynamic network of spatially interchanging and transient environments.

We conducted geophysical surveys along a profile across the fault scarp northeast from the Holy Trinity Monastery (Figure 2). A thin, yellowish soil, developed on sand and gravel of the Lozenets Formation, caps the footwall surface, whereas the hanging wall comprises thick, dark-colored soil developed within clay- and silt-dominated deposits of a Holocene age. Ground conditions were wet during the surveys, though surface ponding within the hanging wall occurred frequently at other times.

3.2. Topographic Profiling

Topographic data for scarp morphometry analysis were collected in the field along a linear transect normal to the fault strike, co-located with the electrode positions of the resistivity survey (Figure 2). Measurements were acquired using a Leica GS18I antenna paired with a CS20 controller. Coordinates were projected to the BGS2005/UTM zone 34 N system (EPSG:7803), achieving horizontal and vertical errors of 2 mm and 3 mm, respectively. Plowing on the flat upper and lower agricultural surfaces represents the ongoing anthropogenic landscape modification. No other artificial terrain alterations affect the profile. Consequently, the measured GNSS-RTK transect provides an accurate representation of fault scarp morphometry, preserving a rare natural scarp within the heavily urbanized Sofia Basin.

Linear regression fits determined slope angles across the linear segments of the profile, where slope breaks delineated individual scarp elements. Following established geomorphic profiling methods (cf., [19]), total scarp height was determined from the vertical separation between the crest and toe. Vertical offset was estimated assuming that the lower original surface is parallel to the upper surface [19].

3.3. Resistivity Profiling

We imaged subsurface apparent resistivity distribution using direct current resistivity profiling. Data acquisition was carried out on 15 July 2025, using an ABEM Terrameter SAS 1000 instrument connected to four 100 m multicore cables and an automated switcher. A total of 101 electrodes were deployed along a 500 m profile at a 5 m minimum spacing. Multi-gradient protocols, implemented using combined Short and Long configurations, exploit

the high sensitivity of gradient geometries to sub-vertical contrasts that strike normal to the profile, here targeting the fault plane [59]. Continuous lateral coverage was maintained through roll-along acquisition, advancing the array center in 100-m increments. Short Multi-Gradient quadripoles added at $x = 100$ m and $x = 400$ m preserved shallow resolution and suppressed edge effects at the profile margins.

We reconstructed subsurface resistivity distributions using the Boundless Electrical Resistivity Tomography v. 2 software [60,61]. The inversion algorithm employed a smoothness-constrained optimization scheme mapped onto a topography-constrained finite-element mesh. Refining the near-surface mesh to a relative cell size of 0.3× the electrode spacing, with spline-smoothed boundaries, preserved numerical precision during forward calculations near electrode positions. The inverse problem was solved using a smoothness-constrained, regularized Gauss-Newton optimization scheme. An anisotropic spatial weighting factor of 0.2 enforced horizontal smoothing relative to vertical variation. This constraint accounts for the predominantly sub-horizontal bedding planes prevailing in both the Neogene footwall and Quaternary hanging wall units, so that the imaged sub-vertical gradients reflect true geological boundaries. The initial regularization strength was set to $\lambda = 40$, a value selected because the overall inversion results remained stable across a range of λ values while sharpening resistivity transitions. Applying a reduction factor of 0.5 across successive iterations stabilized early convergence toward regional trends before progressively resolving sharp localized anomalies. Recalculating the sensitivity matrix (Jacobian) at each iteration maintained numerical stability and accuracy throughout the inversion. Starting from a homogeneous background resistivity of 11 Ωm (the mean apparent resistivity), the inversion converged in three iterations, reaching the target threshold of normalized chi-squared misfit $\chi^2 \leq 1.0$ ($\chi^2 = 0.74$, relative root-mean-square error RRMS = 10.5%) and resolving model resistivity values between 3 Ωm and 81 Ωm.

3.4. Passive Seismic Acquisition and Microseismic Resonance Profiling

Ambient microseismic noise was recorded along a profile co-located with the central portion of the resistivity profile extending from $x = 90$ m to $x = 306$ m (Figure 2). We deployed seven Kinemetrics ETNA-2 three-component digital accelerometers across 12 profile points spaced approximately 20 m apart. Field acquisition took place in two consecutive setups on 5 August 2025: points 1–6 recorded from 05:27 to 07:27 UTC, followed by points 7–12 from 07:51 to 09:51 UTC. We aligned all triaxial sensors orthogonally (X = North, Y = East, Z = Vertical) and recorded continuous wavefields at a sampling rate of $F_s = 100$ Hz.

We segmented continuous vertical-component acceleration records $x_p(t)$ into fixed blocks of $N = 8192$ samples (≈81.92 s) with 50% overlap, yielding a frequency resolution of $\Delta f = 0.0122$ Hz. We linearly detrended each block to remove drift and applied a periodic Hann window $w(n)$ to suppress spectral leakage. Fast Fourier Transforms (FFT) yielded the single-sided amplitude spectrum $|X_p(f, b)|$ normalized by the window's coherent gain ($C_g = \frac{1}{N}\sum_{n=1}^{N} w(n)$):

$$|X_p(f, b)| = \frac{2 \cdot |\mathcal{F}x_{p,b}(n) \cdot w(n)|}{N \cdot C_g}. \quad (1)$$

Dual statistical criteria rejected non-stationary noise transients prior to spectral accumulation. First, we required block RMS amplitude to satisfy $r_{p,b} \leq \text{med}(r_p) + 4.0 \times 1.4826 \times \text{MAD}(r_p)$, where MAD is the median absolute deviation of block RMS amplitudes. Second, we capped Spectral Kurtosis at $K_{p,b} \leq 8.0$ to exclude impulsive broadband events. Across M accepted windows, we calculated the ensemble mean amplitude spectrum $\bar{S}_p(f)$ and its 95% confidence interval:

$$\bar{S}_p(f) = \frac{1}{M}\sum_{b=1}^{M}|X_p(f,b)|, \quad \mathrm{CI}_{95}(f) = \bar{S}_p(f) \pm 1.96\frac{\sigma_p(f)}{\sqrt{M}}, \tag{2}$$

where $\sigma_p(f)$ is the spectral standard deviation. Here, M denotes the total number of accepted windows at a given station. In the convergence analysis below, k denotes the number of sequentially accumulated accepted windows, with $k \leq M$. The resulting ensemble mean amplitude spectra for all 12 measurement stations are shown in Figure 4.

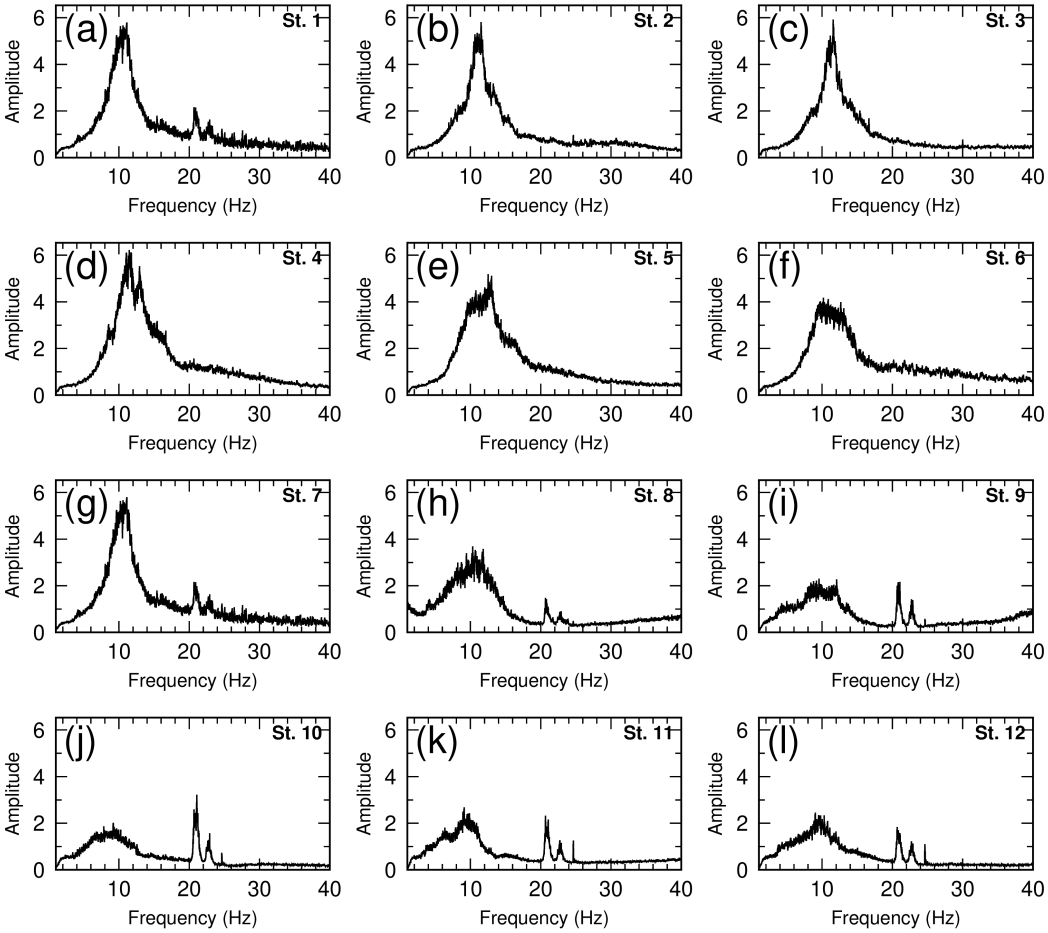

Figure 4. Ensemble mean amplitude spectra $\bar{S}_p(f)$ for stations 1–12 (**a**–**l**).

The algorithm evaluates cumulative spectral stabilization to confirm that peaks reflect stationary resonances. Let $S_k(f) = \frac{1}{k}\sum_{b=1}^{k}|X_p(f,b)|$ denote the spectrum calculated after accumulating k time windows. We defined the relative spectral variation Δ_k between consecutive cumulative spectra using normalized Euclidean distance:

$$\Delta_k = \frac{\|S_k(f) - S_{k-1}(f)\|_2}{\|S_k(f)\|_2}. \tag{3}$$

Averaging a large number of ambient-noise amplitude spectra is a central step of the passive standing-wave approach because persistent resonance peaks are reinforced in the averaged spectrum, whereas temporally variable contributions are reduced [24–27]. We additionally evaluated convergence of the cumulative mean spectrum as a function of the number of accepted windows (Figure 5). The 10% threshold used here is an operational convergence criterion specific to this dataset; it is not treated as a formal test of statistical stationarity. Across the profile, the cumulative spectral estimates progressively approach the final mean spectrum, demonstrating that the principal spectral peaks are persistent over the analyzed recording interval.

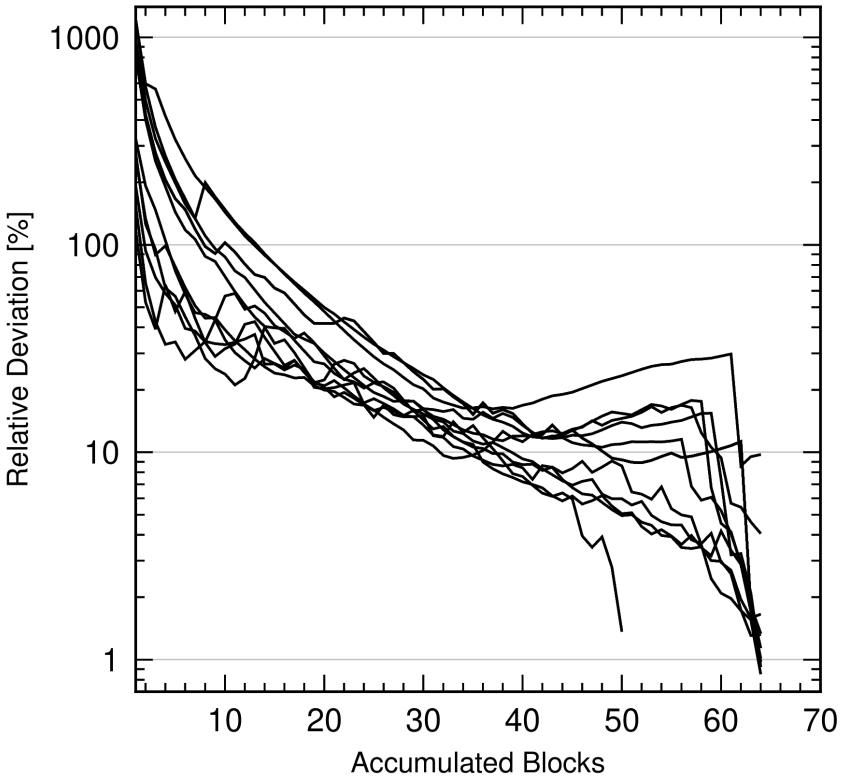

Figure 5. Relative spectral variation Δ_k versus accumulated FFT windows k across all 12 stations.

Once stabilized, each spectral estimate was normalized to its peak amplitude:

$$\hat{S}_n(f) = \frac{\bar{S}_p(f)}{\max\left(\bar{S}_p(f)\right)}. \quad (4)$$

This peak normalization suppresses differences in absolute amplitude scale and emphasizes relative spectral shape, facilitating comparison of the frequency-dependent spectral patterns among stations. The normalized amplitudes therefore represent relative, rather than absolute, measures of site response.

For spatial analysis, the normalized spectra were compiled along the profile coordinates to form a two-dimensional frequency–space spectral field $A(x,f)$, where x is distance along the profile, f is frequency, and A is normalized spectral amplitude ($0 \leq A \leq 1$). This matrix provides frequency–space maps of normalized spectral amplitude that can be displayed against elevation or transformed to an equivalent-depth coordinate for comparative interpretation, and pseudosections projected against both elevation and equivalent depth.

For exploratory depth representation, the frequencies of persistent spectral maxima were converted to quarter-wavelength equivalent depths using

$$H = V_{\mathrm{p}}(H)/4f. \quad (5)$$

This approximation assumes that the selected spectral maximum corresponds to the fundamental compressional resonance of a layer bounded by a free surface and a mechanically contrasting lower interface [24,27,62]. Because the modal order has not been independently established, the resulting pseudodepth coordinate remains conditional on this assumption and on the adopted P-wave velocity model. For visualization in an equivalent-depth coordinate, we applied a 1-D V_{p} model based on representative seismic parameters for the Sofia sedimentary basin [63] (Table 1). The same velocity model was applied at all stations so that lateral differences in the pseudosection arise from the measured spectral response rather than from spatially varying velocity assumptions. The transformation is

used only as a first-order depth representation; the resulting vertical coordinate is therefore treated as quarter-wavelength equivalent depth (pseudodepth), not as independently constrained geological depth.

Table 1. 1D P-wave velocity model used for frequency-to-depth conversion.

Depth (m)	0	2	5	10	20	35	50	75	100
$\boldsymbol{V_p}$ (m/s)	300	340	390	460	560	700	850	1050	1250

To quantify the sensitivity of the equivalent-depth transformation to the assumed *P*-wave velocity model, we performed a three-scenario analysis using the reference 1-D velocity profile in Table 1. The reference velocities were uniformly scaled by factors of 0.8, 1.0, and 1.2, representing lower, nominal, and higher velocity scenarios, respectively. These perturbations were selected as an exploratory sensitivity range rather than a statistically determined uncertainty interval. For each frequency, the implicit quarter-wavelength relation (Equation (5)) was solved numerically, using linear interpolation between the velocity–depth control points.

For the dominant 9–12 Hz band, the nominal model yields equivalent depths of approximately 9.4–13.8 m. The lower-velocity scenario gives 7.0–10.3 m, whereas the higher-velocity scenario gives 12.0–18.0 m. At 10 Hz, the estimated equivalent depth changes from 12.0 m in the reference model to 8.9 m and 15.4 m in the lower- and higher-velocity scenarios, respectively.

The sensitivity analysis demonstrates that the absolute equivalent-depth coordinate depends appreciably on the assumed velocity structure. However, because the same velocity transformation is applied to all stations, the measured lateral variations in spectral amplitude and frequency remain unchanged. The analysis therefore supports the robustness of the observed lateral spectral contrast with respect to the tested velocity perturbations, while confirming the model dependence of its vertical position. The calculation remains conditional on the assumption that the selected frequencies represent fundamental compressional resonance.

4. Results

4.1. Scarp Profile

A degraded normal fault scarp separates two planar surfaces in the topographic profile (Figure 6a). The upper original surface extends from the southern end of the profile to $x = 154$ m. It truncates the Lozenets Formation and slopes at 3.8°. Beyond the northern margin of the upper surface, the slope steepens to 5.4° across a 20 m-wide zone where accelerated erosion caused retreat of the scarp crest.

Downslope, a wash slope spans a total horizontal width of 73 m (174–247 m) with a mean angle of 3.1°. The wash slope comprises three sub-elements: a steep upper slope spanning 7 m (174–181 m) at 8.3°, a 18.5 m-wide depression (181.0–199.5 m) at 5.3°, and a gentle slope extending 47.5 m (199.5–247.0 m) at 3.1°. Beyond the scarp toe at $x = 247$ m, the profile terminates along the lower original surface at a slope angle of 0.9°.

The scarp height is estimated at 8.22 ± 0.34 m (Figure 6a). Uncertainty incorporates elevation measurement errors and a ±5 m positional uncertainty for the toe ($x = 247$ m) and crest ($x = 154$ m) due to profile point spacing. Total vertical offset is 7.00 ± 0.27 m. Because erosion has lowered the scarp crest and wash deposition may have aggraded the surface downslope from the toe on the downthrown block, this measurement represents a minimum estimate of vertical offset from multiple events.

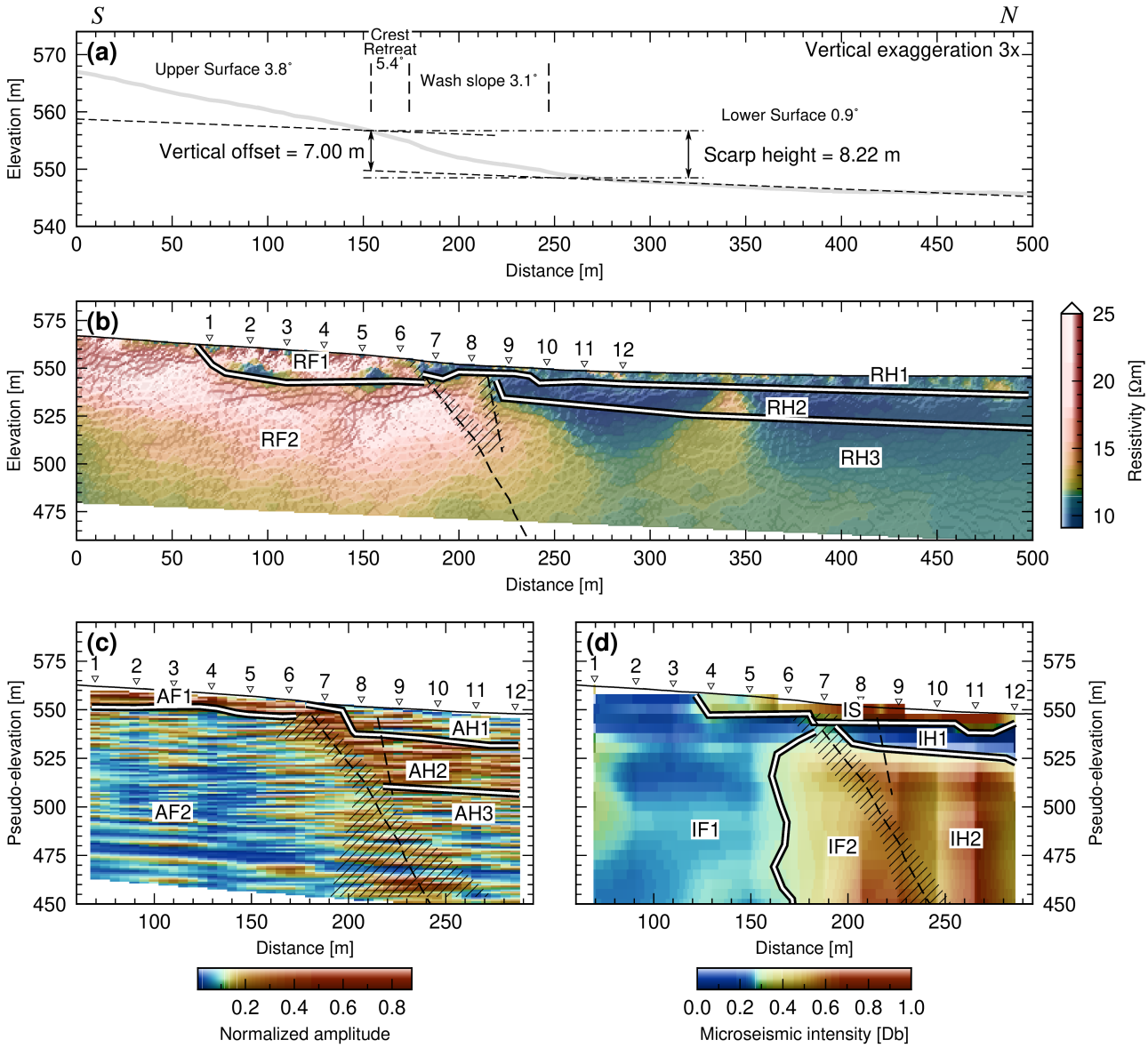

Figure 6. Topographic, resistivity, and passive seismic profiles across the Novi Han fault scarp. (**a**) Surface topographic profile displaying a compound fault scarp with geomorphic elements and projection lines used to determine scarp height and vertical offset. (**b**) Electrical resistivity model; labeled domains (RH1–RH3, RF1–RF2) are outlined in white, and the interpreted fault is indicated by solid black lines. (**c**) Pseudo-section of normalized spectral amplitude featuring outlined and labeled domains. (**d**) Microseismic intensity field modeled by Oynakov et al. [18], showing domains delineated and labeled in this study. Hatched areas in (**b**–**d**) mark lateral transitions indicative of a fault, and dashed lines stand for the inferred fault. Inverted triangles and numbers 1–12 in (**b**–**d**) denote ambient noise measurement stations.

4.2. Resistivity Model

The modeled resistivity reveals a zonal distribution with a central transition beneath the fault scarp (Figure 6a,b). The southern footwall zone comprises domains RF1 and RF2. Shallow domain RF1 consists of two layers: an upper layer that reaches 60 Ωm and a lower conductive layer (10 Ωm). Deep domain RF2 mostly spans 17–21 Ωm and decreases to 13 Ωm at depth. The northern hanging-wall zone comprises domains RH1, RH2, and RH3. The uppermost domain, RH1, forms a 7-m-thick layer whose resistivity varies laterally from 9 to 15 Ωm. Domain RH2 stands out for its high conductivity (8–9 Ωm) despite a single

14 Ωm anomaly at $x \approx 345$ m. Resistivity within deep domain RH3 gradually increases to 12 Ωm.

4.3. Normalized Spectral Amplitude

The normalized spectra show a concentration of spectral amplitude within 9–12 Hz along most of the profile (Figure 7). Persistent spectral peaks obtained by averaging multiple noise records are the primary observational feature used in passive standing-wave studies to identify resonance frequencies [24–27]. We therefore refer to the 9–12 Hz feature conservatively as the dominant resonance band. Its assignment to a specific standing-wave mode would require confirmation from the expected modal frequency sequence and boundary conditions. Additional energy around 18–22 Hz occurs mainly in the northern part of the profile. Because this band is not demonstrated here to follow the expected harmonic sequence of compressional standing-wave modes, it is treated as a secondary spectral-amplitude band rather than as a higher-order mode. The persistence of these spectral features supports their use for comparing the frequency-dependent response between measurement stations, but does not establish their modal order. In particular, the quarter-wavelength depth transformation assumes a fundamental compressional resonance and should therefore be regarded as a conditional representation rather than an independently verified depth conversion. Stations 1–6 in the fault footwall generally exhibit a narrower and more laterally consistent dominant band, whereas stations 7–12 in the fault hanging wall show broader spectral maxima, stronger secondary peaks, and greater station-to-station variability.

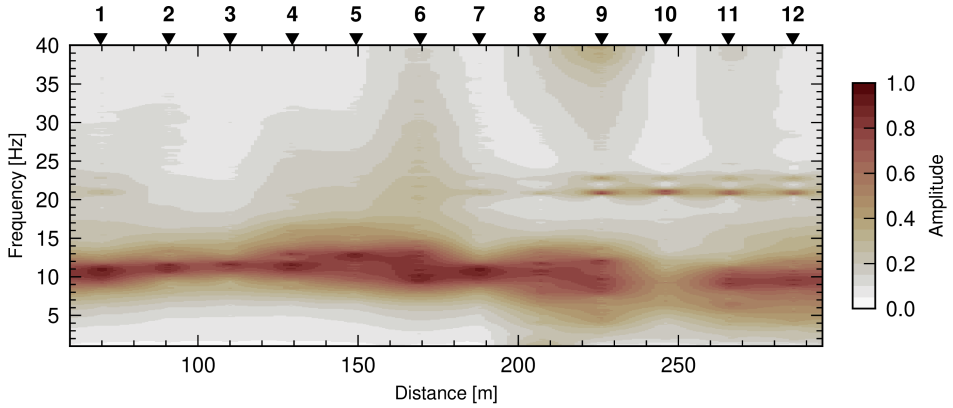

Figure 7. Normalized amplitude spectra across the profile measurement stations (1–12, marked by inverted triangles at the top axis).

Joint visualization of averaged spectra acquired along a profile has previously been used to map the spatial distribution of standing-wave resonance features and their modal amplitudes [23,24,27]. In the present profile, the normalized spectral-amplitude pseudo-section resolves two principal spectral lateral zones separated by a transition between approximately 190 and 240 m along the profile (Figure 6c).

In the southern zone, shallow domain AF1 displays high-amplitude spectral bands ($A > 0.6$) conformable to the surface topography. Below a pseudo-elevation of ~550 m, domain AF2 is characterized by lower amplitudes ($A < 0.3$) interrupted by thin, isolated sub-horizontal spectral maxima. The northern zone comprises three vertically differentiated domains. Shallow domain AH1 exhibits moderate to high amplitudes ($A \approx 0.5$–0.7), intermediate domain AH2 contains relatively continuous high-amplitude bands ($A \approx 0.7$–0.8), and lower domain AH3 displays alternating high- and low-amplitude bands with greater vertical spacing. Within the lateral transition between the two zones of the profile, several sub-horizontal amplitude bands lose continuity or terminate. Across the profile, the vertical

spacing between spectral-amplitude bands generally increases below a pseudo-elevation of approximately 500 m.

5. Discussion

5.1. Geoelectric and Microseismic Interpretation of Shallow Geology

Resistivity methods are widely established and proven in active fault studies (e.g., [7,19,20,64]). Complementing the resistivity profiling, we apply a specific passive seismic standing-wave approach to image a fault zone in detail. Both geophysical models reveal a two-zone pattern with a transition beneath the fault scarp (Figure 6a–c) that captures the variations between fault blocks expected from geological observations at the ground surface. The spatial alignment between the resistivity distribution and the pseudo-elevation spectral amplitude plot confirms the utility of multiple independent geophysical indicators, particularly in the absence of direct V_p logging.

The electrical resistivity tomogram (Figure 6b) defines two main geoelectric zones separated by an inclined transition zone between profile distances 180 and 200 m. The southern footwall block comprises domains RF1 and RF2, which exhibit elevated resistivities fluctuating around 20 Ωm. These values are typical of sand layers within the Lozenets Formation elsewhere in the Sofia Basin (e.g., [7]). Owing to the relatively high resistivity, the clay, silt and gravel layers reported within the local Neogene sequence (e.g., [1,2]) are likely sparse or absent along this profile. Lithology in the footwall domains is uniform at the profile resolution. The elevated conductivity at the base of domain RF1 likely points to localized groundwater saturation.

High conductivity over a narrow resistivity range dominates the hanging-wall basin (Figure 6b). The geoelectric uniformity suggests a homogeneous sediment fill despite facies interdigitation among small alluvial aprons apexed along the fault scarp, footwall-derived colluvial sand and silt, axial river flood deposits [2], and the Iskar fluvial fan. The threefold resistivity layering within an otherwise uniform resistivity background is interpreted to reflect high water saturation within the highly conductive domain RH2. Frequent lateral resistivity variations in the overlying domain RH1 suggest the presence of closely spaced conductive pathways that may facilitate fluid exchange between RH2 and the ground surface. Year-round surface waterlogging and scarp-base springs in the immediate vicinity confirm vertical hydrological connectivity.

We interpret the southward resistivity increase within the hanging wall to an increasing volume of gravel- and sand-enriched colluvial deposits toward the fault scarp. In the shallow subsurface, the fault truncates the substrate beneath the steepest portion of the wash-controlled scarp slope, where elevated resistivities in domain RF2 terminate along a north-dipping linear boundary. At a depth of ~30 m (the investigation depth limit of the Short Multi-gradient Array), the interface between the fault blocks broadens into a transitional zone that obscures a discrete fault trace. The lithological similarity between the juxtaposed fault blocks reduces resistivity contrast, independent of signal sensitivity decay at depth. To resolve ambiguities in the resistivity model, we analyze variations in the ambient-noise spectral response.

The normalized microseismic spectra provide a measure of lateral and vertical changes in the ambient-noise spectral response. The persistence of the dominant 9–12 Hz band along much of the profile, combined with spatial variations in its amplitude and spectral width (Figure 7), suggests that the principal spectral feature is broadly maintained while local subsurface conditions modify its expression. The spectral-amplitude pseudo-section (Figure 6c) shows a lateral partition comparable with that observed in the resistivity model. In the southern footwall zone, shallow high-amplitude domain AF1 overlies lower-amplitude domain AF2. Because RF2 and most of RF1 exhibit relatively uniform resistivity (~20 Ωm),

the spectral contrast between AF1 and AF2 need not represent a major lithological boundary. Instead, the contrast may reflect depth-dependent variations in mechanical properties, compaction, weathering, or fluid saturation within the Lozenets Formation. The conductive interval near the base of RF1 is consistent with increased moisture and may contribute to an elastic-impedance contrast near the AF1–AF2 transition. Changes in fluid saturation provide a physically plausible mechanism for the observed elastic-impedance contrast, and integrating complementary geophysical constraints strengthens this assumption.

In the hanging wall to the north, domain AH1 likely corresponds to shallow layers subjected to uneven soil moisture retention and variable compaction, showing a spatial correlation with resistivity domain RH1. The near-surface elastic contrasts support moderate to high standing-wave resonance within the uppermost meters.

The underlying domain AH2 contains relatively continuous high-amplitude spectral bands and coincides with the conductive domain RH2. This spatial correspondence suggests that the spectral response is likely sensitive to the physical conditions responsible for the high conductivity. Increased water content may modify density and elastic properties and thereby alter seismic impedance contrasts within the sedimentary sequence. The observed spectral amplitudes indicate sensitivity to fluid saturation, depositional layering, and compaction, though isolating the governing mechanism requires complementary constraints.

In the lowermost domain AH3 within the hanging wall, alternating amplitude bands display wider vertical spacing beneath pseudo-elevation ~505 m. Although rising lithostatic overburden increases compaction, the higher clay content in the hanging wall preserves distinct inter-bed impedance contrasts against silty or sandy interbeds. Compared to the stiffer, uniform sand unit of the footwall, the lower bulk and shear moduli of the clay-rich matrix, coupled with elevated capillary moisture retention, maintain the strong elastic contrasts necessary to drive higher resonant amplitudes at lower frequencies.

The lateral termination and reduced continuity of spectral-amplitude bands within the transition zone coincide spatially with the fault position constrained independently by topography and resistivity. Previous passive standing-wave studies demonstrate that changes in boundary geometry and acoustic contrast modify the spatial distribution of resonance peaks and amplitudes [24,26,27]. We therefore interpret the reduced lateral continuity of the spectral-amplitude bands as being consistent with interrupted stratification. While these spectral amplitudes capture the broad physical properties of the fault zone, finer-scale fault geometry remains outside the resolution of the method.

The sensitivity analysis provides a quantitative estimate of the influence of the assumed P-wave velocity model on the equivalent-depth representation. Uniform velocity perturbations of ±20% shift the estimated depths associated with the dominant 9–12 Hz band from the nominal interval of 9.4–13.8 m to 7.0–10.3 m and 12.0–18.0 m, respectively. These differences demonstrate that the converted depths should not be treated as independently measured geological interface depths. The principal lateral spectral transition is nevertheless present in the original frequency–distance representation and does not depend on the velocity model. Its correspondence with the resistivity transition therefore provides evidence of a lateral change in subsurface physical properties independently of the assumed pseudodepth scale. The sensitivity analysis does not, however, establish the absolute depth, dip, or detailed geometry of the fault plane.

5.2. Comparison with Microseismic Energy Distribution Model

Oynakov et al. [18] reconstructed the passive seismic energy distribution using the same microseismic dataset as in our standing-wave amplitude calculations. To facilitate comparison with our models, we delineate domains of relatively uniform patterns across the profile of Oynakov et al. [18] (Figure 6d). The microseismic intensity pseudo-section resolves a

sub-vertical boundary extending through the entire depth near the 170-m mark (Figure 6d). The boundary juxtaposes domain IF1 ($I < 0.3$ dB) with domain IF2 ($I \approx 0.4$–0.6 dB). This boundary is absent in the electrical resistivity and standing-wave amplitude models (Figure 6b,c). A shallow domain IS ($I \approx 0.6$–0.8 dB) caps the northern sector of the pseudo-section and extends southward across the fault. Beneath IS, domain IH1 forms a continuous sub-horizontal layer of minimal intensity ($I < 0.2$ dB). At depth in the fault hanging wall, lowermost domain IH2 displays high to very high intensity ($I \approx 0.7$–1.0 dB) partitioned into vertical to sub-vertical bands.

We attribute the signal attenuation in domain IF1 (Figure 6d) to elevated seismic wave velocities within compacted Neogene sands. Domain IH1 also exhibits low microseismic intensity ($I < 0.2$ dB). Its spatial coincidence with the low-resistivity domain RH2 leads us to consider the hypothesis of localized fluid accumulation. Pore-fluid saturation increases compressional wave velocity and generates fluid friction that dampens seismic waves. Energy loss suppresses the ambient signal and produces the low microseismic intensity observed in domain IH1. Because domain IH1 represents a fluid-saturated horizon, it extends across the fault and transitions into domain IF1 without indicating a depositional change. The strong acoustic impedance contrast at the water table traps shallow wavefield energy and drives localized microseismic intensity amplification ($I \approx 0.6$–0.8 dB) continuously across both footwall and hanging wall. We attribute the high intensity in domain IH2 to energy trapping against the moderately dipping fault plane. Inclined at ~60°, the fault boundary may acts as an effective acoustic reflector relative to the overlying Quaternary fill and may focus vertical body-wave amplification within the hanging wall. A low-velocity gouge layer could further enhance this impedance contrast.

Microseismic intensity zone IF2 lies beneath the dipping boundary that correlates with the fault imaged in both resistivity and standing-wave amplitude models. Neither resistivity nor standing-wave amplitude displays disruption across the sub-vertical IF1–IF2 transition. The lack of complementary geophysical evidence indicates that IF2 does not represent a distinct geological or mechanical unit. We suggest that refraction focusing and boundary-wave leakage along the moderately dipping fault plane concentrate seismic energy, generating IF2 as a sub-fault wavefield focusing effect. The elevated intensity in IF2 contrasts with the low values of the footwall Neogene sands (IF1) and falsely mimics the high intensity of hanging-wall zone IH2. It should be emphasized that the sub-fault wavefield focusing effect observed in domain IF2 enhances fault-plane resolution at depths beyond ~30 m, where resistivity model sensitivity degrades due to the penetration limit of the Short Multi-gradient Array. Further refining the microseismic intensity technique requires denser station spacing above the expected fault plane and the establishment of diagnostic criteria to identify sub-fault wavefield focusing effects.

5.3. Fault System Connectivity

Our findings along the Novi Han fault segment show that individual fault displacements at the studied site must be sufficiently large to yield a vertical offset of 7 m, while scarp crest retreat points to a long elapsed time since the most recent surface rupture. Consequently, the Novi Han segment likely did not rupture the surface in 1858, except for potential minor ground effects. This local inference, combined with the requirement of substantial fault displacement for scarp formation, aligns with the working hypothesis that the southern fault system may undergo partial ruptures instead of releasing its entire seismic moment in a single characteristic event. This mechanism could apply regardless of whether the fault system ruptures through laterally segmented events or through complete ruptures with a slip distribution that fails to rupture the ground surface everywhere. While testing system-wide segmentation requires broader paleoseismic data across multiple sites,

our local site observations suggest that seismic source models considering single- or multi-segment ruptures deserve further evaluation. Such fault heterogeneity, stemming from long-term orogenic evolution and non-orthogonal extension, frequently favors variable segment ruptures and recurrence intervals (e.g., [65,66]).

6. Conclusions

This study integrates high-resolution topographic scarp morphometry, electrical resistivity profiling, and vertical-component ambient-noise standing-wave profiling to refine the near-surface geology of the Novi Han fault segment. Topographic measurements reveal an 8.22 m high compound scarp with 7 m of total vertical offset. Scarp crest retreat indicates a long elapsed time since the last surface-rupturing event. Co-located resistivity and passive spectral-amplitude models independently delineate a north-dipping fault that separates the footwall Neogene Lozenets Formation from Quaternary hanging-wall fill. The close agreement between model features shows that standing-wave resonance features resolve fluid saturation and elastic-impedance contrasts with sufficient accuracy for geological interpretation, even without direct V_p constraints. Comparison confirms that the microseismic intensity model of Oynakov et al. [18] aligns well with our resistivity and ambient-noise standing-wave models, as all three capture the main geological variations. Crucially, the microseismic intensity model reveals a sub-fault wavefield focusing effect that creates a sub-vertical boundary beneath the surface fault trace with no equivalent in the other models. This phenomenon enhances the resolution of the fault plane at depths greater than ~30 m, compensating for the degraded sensitivity of the resistivity model at depth.

Placed in a basin-wide context, our results suggest that the Novi Han fault segment either did not rupture the ground surface in the 1858 earthquake or underwent surface displacement too negligible to be detected at the 5 m profile spacing used. Historical accounts and our results point to partial rupture scenarios. We conclude that seismic hazard models for the Sofia Basin should consider partial-rupture behaviors alongside system-size characteristic events to better account for fault heterogeneity.

Author Contributions: Conceptualization, A.R. and E.O.; methodology, A.R. and E.O.; validation, R.I. and L.P.; formal analysis, A.R. and E.O.; investigation, A.R., E.O., Y.D., L.P., P.K. and R.I.; resources, A.R., E.O., L.P. and R.I.; data curation, A.R., E.O. and L.P.; writing—original draft preparation, A.R. and E.O.; writing—review and editing, R.I. and L.P.; visualization, A.R. and E.O.; project administration, R.I.; funding acquisition, R.I. and L.P. All authors have read and agreed to the published version of the manuscript.

Funding: This research was conducted within the framework of the project "Assessment of earthquake ground motion amplification in the Sofia Basin", funded by the Bulgarian National Science Fund under Grant No. КП-06-Н64/1 (15 December 2022).

Institutional Review Board Statement: Not applicable.

Informed Consent Statement: Not applicable.

Data Availability Statement: The data presented in this study are openly available in Zenodo at https://doi.org/10.5281/zenodo.22831553 [67].

Acknowledgments: We are grateful to three anonymous reviewers for their careful reading of our work and their valuable advice on improving it.

Conflicts of Interest: The authors declare no conflicts of interest.

Abbreviations

The following abbreviations are used in this manuscript:

FFT	Fast Fourier Transform
GNSS	Global Navigation Satellite System
MAD	Median Absolute Deviation
RMS	Root Mean Square
RRMS	Relative Root-Mean-Square
RTK	Real-Time Kinematic
UTC	Coordinated Universal Time

References

1. Kanev, D. Morphologie du versant septentrional et du pied de la montagne de Lozene. *Annu. Sofia Univ. Fac. Biol. Geol. Geogr. Book 3—Geogr.* **1956**, *49*, 104–122. (In Bulgarian)
2. Kanev, D. On the baselevel response to the gully formation in the south-eastern part of Sofia plain. *Annu. Univ. Sofia Fac. Geol. Geogr. Livre 3—Geogr.* **1962**, *55*, 97–106. (In Bulgarian)
3. Vrablianski, B. On the neotectonic activation of the fault structures in Bulgaria. *Geotecton. Tectonophys. Geodyn. (Bulg. Acad. Sci.)* **1975**, *2*, 15–26. (In Bulgarian)
4. Alexiev, G.; Georgiev, T. Morphotectonics and seismic activity of the Sofia depression. *Probl. Geogr. (Bulg. Acad. Sci.)* **1997**, *1–2*, 60–69. (In Bulgarian)
5. Shanov, S.; Tzankov, T.; Nikolov, G.; Boykova, A.; Kourtev, K. Characters of the recent geodynamics of the Sofia Complex Graben. *Rev. Bulg. Geol. Soc.* **1998**, *59*, 3–12.
6. Kotzev, V.; Nakov, R.; Georgiev, T.; Burchfiel, B.C.; King, R.W. Crustal motion and strain accumulation in western Bulgaria. *Tectonophysics* **2006**, *413*, 127–145. [CrossRef]
7. Radulov, A.; Donkova, Y.; Yaneva, M.; Nikolov, N. Multiple ruptures on the North-Sofia fault at Gorni Bogrov from scarp profile and shallow geophysics. *Geol. Balc.* **2023**, *52*, 65–74. [CrossRef]
8. Burchfiel, C.B.; Nakov, R.; Tzankov, T.; Royden, L.H. Cenozoic extension in Bulgaria and northern Greece: The northern part of the Aegean extensional regime. *Geol. Soc. Lond. Spec. Publ.* **2000**, *173*, 325–352. [CrossRef]
9. Caporali, A.; Aichhorn, C.; Barlik, M.; Becker, M.; Fejes, I.; Gerhatova, L.; Ghitau, D.; Grenerczy, G.; Hefty, J.; Krauss, S.; et al. Surface kinematics in the Alpine–Carpathian–Dinaric and Balkan region inferred from a new multi-network GPS combination solution. *Tectonophysics* **2009**, *474*, 295–321. [CrossRef]
10. Kamenov, B.; Kojumdgieva, E. Stratigraphy of the Neogene in the Sofia Basin. *Palaeontol. Stratigr. Lithol. (Bulg. Acad. Sci.)* **1983**, *18*, 69–85. (In Bulgarian)
11. Yaneva, M.; Berov, B.; Frangov, G. Evolution of Sofia Basin during the Neogene. *Geol. Balc.* **2002**, *32*, 135–138. [CrossRef]
12. Zagorčev, I.S. Neotectonics of the central parts of the Balkan Peninsula: Basic features and concepts. *Geol. Rundsch.* **1992**, *81*, 635–654. [CrossRef]
13. D'Agostino, N.; Métois, M.; Koci, R.; Duni, L.; Kuka, N.; Ganas, A.; Georgiev, I.; Jouanne, F.; Kaludjerovic, N.; Kandić, R. Active crustal deformation and rotations in the southwestern Balkans from continuous GPS measurements. *Earth Planet. Sci. Lett.* **2020**, *539*, 116246. [CrossRef]
14. Radulov, A.; Rockwell, T.K.; Yaneva, M.; Donkova, Y.; Kiselinov, H.; Nikolov, N. Variable slip mode in the past 3300 years on the fault ruptured in the 2012 M 5.6 Pernik slow earthquake in Bulgaria. *Nat. Hazards* **2024**, *120*, 5309–5331. [CrossRef]
15. Oynakov, E.; Ivanov, R.; Dimitrova, L.; Radulov, A. Evaluation and analysis of microseismic records on the territory of the Sofia Basin. *J. Theor. Appl. Mech.* **2024**, *54*, 429–445. [CrossRef]
16. Danciu, L.; Nandan, S.; Reyes, C.; Basili, R.; Weatherill, G.; Beauval, C.; Rovida, A.; Vilanova, S.; Sesetyan, K.; Bard, P.Y.; et al. *The 2020 Update of the European Seismic Hazard Model: Model Overview*; EFEHR Technical Report 001, v1.0.0. Technical report; EFEHR European Facilities of Earthquake Hazard and Risk: Zurich, Switzerland, 2021. [CrossRef] [PubMed]
17. Guéorguiev, M. Géomorphologie du versant sud de la montagne Mourgach entre les villages Jéliava et Négouchevo. *Annu. Univ. Sofia, Fac. Geol. Geogr.* **1968**, *62*, 53–70. (In Bulgarian)
18. Oynakov, E.; Pashova, L.; Kirilov, P.; Popova, M.; Ivanov, R. Integrated passive-seismic investigation of a presumed fault-related anomaly north of Lozen Mountain, Sofia Basin. *Geotechnics* **2026**, *6*, 74 . [CrossRef]
19. Improta, L.; Ferranti, L.; De Martini, P.M.; Piscitelli, S.; Bruno, P.P.; Burrato, P.; Civico, R.; Giocoli, A.; Iorio, M.; D'Addezio, G.; et al. Detecting young, slow-slipping active faults by geologic and multidisciplinary high-resolution geophysical investigations: A case study from the Apennine seismic belt, Italy. *J. Geophys. Res. Solid Earth* **2010**, *115* , B11307. [CrossRef]
20. Štěpančíková, P.; Stemberk, J.; Tábořík, P.; Fischer, T.; Findžová, L.; Valenta, J. Discovering the Čirá–Kopanina fault: Bridging the gap between surface evidence and seismic activity. *Lithosphere* **2025**, *2024*, lithosphere_2024_192. [CrossRef]

21. Xu, R.; Wang, L. The horizontal-to-vertical spectral ratio and its applications. *EURASIP J. Adv. Signal Process.* **2021**, *2021*, 75. [CrossRef]
22. Snieder, R.; Trampert, J. Inverse problems in geophysics. In *Wavefield Inversion*; Springer: Berlin/Heidelberg, Germany, 1999; pp. 119–190.
23. Feng, Y.; Chen, Y.; Feng, S.; Jin, P.; Liu, Z.; Lin, Y. An intriguing property of geophysics inversion. In *Proceedings of the International Conference on Machine Learning*; PMLR: Cambridge, MA, USA, 2022; pp. 6434–6446.
24. Kolesnikov, Y.I.; Fedin, K.V. Detecting underground cavities using microtremor data: Physical modelling and field experiment. *Geophys. Prospect.* **2018**, *66*, 342–353. [CrossRef]
25. Kolesnikov, Y.; Fedin, K. Determination of resonant properties of near-surface layer using microtremor data. In Proceedings of the EAGE-GSM 2nd Asia Pacific Meeting on Near Surface Geoscience and Engineering, Kuala Lumpur, Malaysia, 22–26 April 2019; Volume 2019, pp. 1–5. [CrossRef]
26. Fedin, K.V.; Kolesnikov, Y.I.; Ngomayezwe, L. Mapping of underground cavities by the passive seismic standing waves method: The case study of Barsukovskaya cave (Novosibirsk region, Russia). *Geophys. Prospect.* **2021**, *69*, 167–179. [CrossRef]
27. Ngomayezwe, L.; Kolesnikov, Y.I.; Fedin, K.V. Diagnostics of asphalt pavement using elastic standing waves. *Near Surf. Geophys.* **2022**, *20*, 82–93. [CrossRef]
28. Shterev, K.D. The hydrogeothermal basin of Sofia Graben (Bulgaria). *Environ. Geol.* **2004**, *46*, 651–660. [CrossRef]
29. Gerdjikov, I.; Dinev, Y.; Vangelov, D. Structural geology of the central part of Kamenitsa-Rakovitsa fault zone. *Annu. Univ. Min. Geol.* **2020**, *63*, 214–219.
30. Bončev, S. Pourquoi le versant nord du Balkan Occidental et le versant sud du Balkan Central sont-ils plus abrupts que les vessants respectifs opposes? *Annu. Univ. Sofia Fac. Phys. Math.* **1927**, *23*, 157–180. (In Bulgarian)
31. Dabovski, C.; Boyanov, I.; Khrischev, K.; Nikolov, T.; Sapunov, I.; Yanev, Y.; Zagorchev, I. Structure and Alpine evolution of Bulgaria. *Geol. Balc.* **2002**, *32*, 9–15. [CrossRef]
32. Vangelov, D.; Gerdjikov, Y.; Kounov, A.; Lazarova, A. The Balkan Fold-Thrust Belt: An overview of the main features. *Geol. Balc.* **2013**, *42*, 29–47. [CrossRef]
33. Ivanov, Z. *Tectonics of Bulgaria*; University Publishing House 'St. Kliment Ohridski': Sofia, Bulgaria, 2017. (In Bulgarian)
34. Schmid, S.M.; Fügenschuh, B.; Kounov, A.; Maţenco, L.; Nievergelt, P.; Oberhänsli, R.; Pleuger, J.; Schefer, S.; Schuster, R.; Tomljenović, B.; et al. Tectonic units of the Alpine collision zone between Eastern Alps and Western Turkey. *Gondwana Res.* **2020**, *78*, 308–374. [CrossRef]
35. Georgiev, N.; Henry, B.; Jordanova, N.; Froitzheim, N.; Jordanova, D.; Ivanov, Z.; Dimov, D. The emplacement mode of Upper Cretaceous plutons from the southwestern part of the Sredna Gora Zone (Bulgaria): Structural and AMS study. *Geol. Carpathica* **2009**, *60*, 15–33. [CrossRef]
36. Nemec, W.; Muszyński, A. Volcaniclastic alluvial aprons in the Tertiary of Sofia District (Bulgaria). *Ann. Soc. Geol. Pol.* **1982**, *52*, 239–303.
37. Nakov, R.; Burchfiel, B.C.; Tzankov, T.; Royden, L.H. *Late Miocene to Recent Sedimentary Basins of Bulgaria*; Geological Society of America Map and Chart Series, MCH088; Geological Society of America: Boulder, CO, USA, 2001.
38. Ognjanova-Rumenova, N.; Yaneva, M.; Botev, I. Paleoecological development of the Sofia Neogene Basin (Southwestern Bulgaria) based on sedimentological and paleontological evidence. *Geol. Carpathica* **2008**, *59*, 59–70.
39. Raffi, I.; Wade, B.S.; Pälike, H.; Beu, A.G.; Cooper, R.; Crundwell, M.P.; Krijgsman, W.; Moore, T.; Raine, I.; Sardella, R.; et al. Chapter 29—The Neogene Period. In *Geologic Time Scale 2020*; Gradstein, F.M., Ogg, J.G., Schmitz, M.D., Ogg, G.M., Eds.; Elsevier: Amsterdam, The Netherlands, 2020; pp. 1141–1215. [CrossRef]
40. Gibbard, P.L.; Head, M.J. Chapter 30—The Quaternary Period. In *Geologic Time Scale 2020*; Gradstein, F.M., Ogg, J.G., Schmitz, M.D., Ogg, G.M., Eds.; Elsevier: Amsterdam, The Netherlands, 2020; pp. 1217–1255. [CrossRef]
41. Andreescu, I.; Codrea, V.; Enache, C.; Lubenescu, V.; Munteanu, T.; Petculescu, A.; Ştiucă, E.; Terzea, E. Reassessment of the Pliocene/Pleistocene (Neogene/Quaternary) boundary in the Dacian Basin (Eastern Paratethys), Romania. *Olt. Stud. Commun. Ştiinţele Nat.* **2011**, *27*, 197–220.
42. Popov, S.V.; Shcherba, I.G.; Ilyina, L.B.; Nevesskaya, L.A.; Paramonova, N.P.; Khondkarian, S.O.; Magyar, I. Late Miocene to Pliocene palaeogeography of the Paratethys and its relation to the Mediterranean. *Palaeogeogr. Palaeoclimatol. Palaeoecol.* **2006**, *238*, 91–106. [CrossRef]
43. Petrov, V. Hydrogeology of the Pliocene Aquifer in the Sofia Basin. Ph.D. Thesis, University of Mining and Geology "St. Ivan Rilski", Sofia, Bulgaria, 2004. (In Bulgarian)
44. Ilieva, M.; Jossifov, D. Structure of the Preneogene basement in the Sofia Depression. *Bulg. Geophys. J.* **1998**, *24*, 109–122. (In Bulgarian)
45. Matova, M.; Spiridonov, H.; Rangelov, B.; Petrov, P. Major active faults in Bulgaria. *J. Earthq. Predict. Res.* **1996**, *5*, 436–439.

46. Basili, R.; Kastelic, V.; Demircioglu Tumsa, M.B.; Garcia Moreno, D.; Nemser, E.S.; Petricca, P.; Sboras, S.P.; Besana-Ostman, G.M.; Cabral, J.; Camelbeeck, T.; et al. *European Database of Seismogenic Faults (EDSF) Compiled in the Framework of the Project SHARE*; Istituto Nazionale di Geofisica e Vulcanologia: Rome, Italy, 2013. [CrossRef]
47. Zelenin, E.; Bachmanov, D.; Garipova, S.; Trifonov, V.; Kozhurin, A. The Active Faults of Eurasia Database (AFEAD): The ontology and design behind the continental-scale dataset. *Earth Syst. Sci. Data* **2022**, *14*, 4489–4503. [CrossRef]
48. Paskaleva, I.; Matova, M.; Frangov, G. Expert assessment of the displacements provoked by seismic events: Case study for the Sofia Metropolitan Area. *Pure Appl. Geophys.* **2004**, *161*, 1265–1283. [CrossRef]
49. Radeva, S.; Paskaleva, I.; Radev, D.; Panza, G. Site dependent estimation of the seismic strong motion—Case study for Sofia region. *Acta Geod. Geophys. Hung.* **2006**, *41*, 395–407. [CrossRef]
50. Piña-Valdés, J.; Socquet, A.; Beauval, C.; Doin, M.P.; D'Agostino, N.; Shen, Z.K. 3D GNSS velocity field sheds light on the deformation mechanisms in Europe: Effects of the vertical crustal motion on the distribution of seismicity. *J. Geophys. Res. Solid Earth* **2022**, *127*, e2021JB023451. [CrossRef]
51. Métois, M.; Lasserre, C.; Méridi, A.; Henriquet, M.; Bodin, T. Bayesian estimation of surface strain rates in the Peri-Adriatic, Balkans and Aegean region from GNSS velocities. *Tektonika* **2025**, *3*, 82–98. [CrossRef]
52. Filaretov, S. Earthquake in Sofia. *Tzarigrad Newsp.* **1858**, *9*, 2. (In Bulgarian)
53. Antonov, D.; Ivanova, K.; Benderev, A.; Djunakova, D.; Yordanov, T.; Kolev, S.; Kunovska, B. Assessment of radon potential along local fault system in Sofia, Bulgaria (at specific test site). *C. R. Acad. Bulg. Sci.* **2024**, *77*, 543–550. [CrossRef]
54. Antonov, D.; Toleva, T.; Burdin, B.; Georgiev, S.V.; Grötsch, J. First data on elevated natural hydrogen occurrence at a site in SE Sofia, Bulgaria. *Rev. Bulg. Geol. Soc.* **2025**, *86*, 76–79. [CrossRef]
55. Solakov, D.E.; Stefanov, D.; Simeonova, S.; Raykova-Tsankova, P. Seismic risk assessment for the city of Sofia, Bulgaria. *Geosciences* **2024**, *14*, 307. [CrossRef]
56. Vanneste, K.; Radulov, A.; De Martini, P.M.; Nikolov, G.; Petermans, T.; Verbeeck, K.; Camelbeeck, T.; Pantosti, D.; Dimitrov, D.; Shanov, S. Paleoseismologic investigation of the fault rupture of the 14 April 1928 Chirpan earthquake (M 6.8), southern Bulgaria. *J. Geophys. Res. Solid Earth* **2006**, *111* , B01303. [CrossRef]
57. Meyer, B.; Sébrier, M.; Dimitrov, D. Rare destructive earthquakes in Europe: The 1904 Bulgaria event case. *Earth Planet. Sci. Lett.* **2007**, *253*, 485–496. [CrossRef]
58. Radulov, A.; Dilov, T.; Rockwell, T.K.; Štěpančíková, P.; Yaneva, M.; Donkova, Y.; Stemberk, J.; Sana, H.; Nikolov, N. First paleoseismic data from the Balkan Range. *Tectonophysics* **2023**, *863*, 230009. [CrossRef]
59. Zonge, K.; Wynn, J.; Urquhart, S. Resistivity, induced polarization, and complex resistivity. In *Near-Surface Geophysics*; Butler, D.K., Ed.; Society of Exploration Geophysicists: Houston, TX, USA, 2005; pp. 265–300. [CrossRef]
60. Günther, T.; Rücker, C.; Spitzer, K. Three-dimensional modelling and inversion of DC resistivity data incorporating topography—II. Inversion. *Geophys. J. Int.* **2006**, *166*, 506–517. [CrossRef]
61. Rücker, C.; Günther, T.; Spitzer, K. Three-dimensional modelling and inversion of DC resistivity data incorporating topography—I. Modelling. *Geophys. J. Int.* **2006**, *166*, 495–505. [CrossRef]
62. Kramer, S.L. *Geotechnical Earthquake Engineering*; Prentice Hall: Upper Saddle River, NJ, USA, 1996.
63. Ivanov, P. Engineering geological conditions in the Sofia Kettle and consequences from the earthquakes. *Geol. Balc.* **2002**, *32*, 117–121. [CrossRef]
64. Suzuki, K.; Toda, S.; Kusunoki, K.; Fujimitsu, Y.; Mogi, T.; Jomori, A. Case studies of electrical and electromagnetic methods applied to mapping active faults beneath the thick Quaternary. In *Engineering Geological Advances in Japan for the New Millennium*; Kanaori, Y., Tanaka, K., Chigira, M., Eds.; Elsevier: Amsterdam, The Netherlands, 2000; Volume 84, pp. 29–45. [CrossRef]
65. Barbot, S.; Lapusta, N.; Avouac, J.P. Under the hood of the earthquake machine: Toward predictive modeling of the seismic cycle. *Science* **2012**, *336*, 707–710. [CrossRef]
66. Scholz, C.H. *The Mechanics of Earthquakes and Faulting*, 3rd ed.; Cambridge University Press: Cambridge, UK, 2019.
67. Radulov, A.; Oynakov, E.; Donkova, Y.; Pashova, L.; Kirilov, P.; Ivanov, R. *Microseismic Noise Acceleration Dataset and DC Resistivity Dataset*; [Dataset]; National Institute of Geophysics, Geodesy and Geography: Sofia, Bulgaria; Geological Institute—Bulgarian Academy of Sciences: Sofia, Bulgaria, 2026. [CrossRef]

Disclaimer/Publisher's Note: The statements, opinions and data contained in all publications are solely those of the individual author(s) and contributor(s) and not of MDPI and/or the editor(s). MDPI and/or the editor(s) disclaim responsibility for any injury to people or property resulting from any ideas, methods, instructions or products referred to in the content.